VIRTUAL AND PHYSICAL PROTOTYPING
2023, VOL. 18, NO. 1, e2273309 (16 pages)
https://doi.org/10.1080/17452759.2023.2273309

Multi Jet Fusion of surface-modified ZnO nanorod–reinforced PA12 nanocomposites

Ran An [a,b]*, Yanbei Hou [a,b]*, Pengfei Tan[a,b], Mei Chen[a,b], Lihua Zhao[a,c] and Kun Zhou [a,b]

[a]HP-NTU Digital Manufacturing Corporate Lab, School of Mechanical and Aerospace Engineering, Nanyang Technological University, Singapore, Singapore; [b]Singapore Centre for 3D Printing, School of Mechanical and Aerospace Engineering, Nanyang Technological University, Singapore, Singapore; [c]3D Lab, HP Labs, HP Inc., Palo Alto, CA, USA

ABSTRACT

Metal oxide nanorods exhibit promising potential as reinforcement fillers in various polymer matrices, but their application in the Multi Jet Fusion (MJF) technique is rarely reported. In this work, surface-modified zinc oxide nanorods (SMZnO) were synthesized and incorporated into polyamide 12 (PA12) powder to enhance the mechanical properties of the MJF-printed parts. Compared to ZnO, SMZnO exhibited better dispersion, resulting in markedly enhanced mechanical performances. The ultimate tensile strength and the Young's modulus of the MJF-printed SMZnO/PA12 nanocomposites were 62.02 MPa and 2.28 GPa in the *X* orientation and 64.07 MPa and 2.34 GPa in the *Y* orientation, equivalent to 27.85%, 59.44%, 29.12%, and 54.97% increments, respectively. The flexural strength and modulus demonstrated similar improvements in the *X* and *Y* orientations, confirming the uniform mechanical enhancement effect of homogenously distributed SMZnO. This work provides a novel and facile approach for the additive manufacturing of polymeric nanocomposites with superior mechanical performance.

ARTICLE HISTORY
Received 5 October 2023
Accepted 15 October 2023

KEYWORDS
Multi Jet Fusion; 3D printing; polyamide 12; metal oxide nanoparticle; mechanical reinforcement; surface modification

1. Introduction

Powder bed fusion (PBF) is an additive manufacturing technology that has attracted both research and industrial attention for the support-free fabrication of polymeric parts with structural complexity and superior mechanical properties [1]. In particular, the Multi Jet Fusion (MJF) technique exhibits unparalleled advantages in the rapid manufacturing of polymeric components as it combines the thermal inkjet system and PBF [2]. An infrared (IR) lamp selectively fuses polymer powder particles that are deposited with a dark-coloured fusing agent (FA), while the powder particles in the surrounding regions do not encounter significant temperature elevation and are thus highly recyclable. Currently, producing composite powder feedstocks that contain reinforcement fillers is the most adopted approach for PBF techniques. The composite powders can be prepared by mechanical mixing, dissolution-precipitation, *in situ* polymerisation, melt-emulsification, *etc* [3–6]. Polyamide 12 (PA12) is one of the most widely adopted semicrystalline thermoplastic materials for PBF processes owing to its high dimensional stability, wide sintering window, and desirable mechanical properties [7,8]. However, the mechanical strengths exhibited by pure PA12 components often fail to meet the stringent requirements of industries such as aerospace, automotive, and sports. Thus, filler-reinforced polymeric composites are studied for the unique and enhanced mechanical properties that are unattainable by their pristine counterparts.

Owing to the selective IR absorption mechanism of MJF printing, only composite powders filled with light-coloured fillers are printable *via* MJF, rendering dark-coloured fillers such as carbon-based fillers, metal nanoparticles, and coloured fibres difficult to process *via* MJF at high filler loading fractions [9–13]. The commercially available glass bead (GB)/PA12 powder demonstrated improved tensile modulus at the expense of the tensile strength of the printed parts. Several types of premixed PA12-based composite powders for the MJF printing of polymeric composites have been reported, including PA12 powders filled with glass fibres (GFs) [14–16], aramid fibres (AFs) [13,17,18], polyimide (PI) fibres [19], and GF–GB hybrids [20]. Taking advantage of the shear-induced fibre alignment during the powder recoating process, the fibre-reinforced composite parts exhibit excellent mechanical

CONTACT Kun Zhou kzhou@ntu.edu.sg Nanyang Technological University, 50 Nanyang Avenue, Singapore 639798, Singapore
*The authors contributed equally to this work.
Supplemental data for this article can be accessed online at https://doi.org/10.1080/17452759.2023.2273309.

properties in the fibre alignment direction, at the cost of deteriorated mechanical properties in other orientations [21,22]. This anisotropy significantly limits the application space of MJF-printed fibre-reinforced parts in applications that require uniform stress distribution.

The surface modification of the reinforcement fillers is an essential strategy to enhance the adhesion between the fillers and the polymers and to improve the powder processability, filler dispersion, and mechanical properties of the final parts [23]. Physically modified fillers possess rough surfaces, effectively promoting the mechanical interlocking between the reinforcement fillers and the polymer matrix [24], while chemically modified fillers are grafted with functional groups that enhance the filler–matrix compatibility [17,23].

Metal oxide nanoparticles, owing to their high surface area to volume ratio, show significant potential in the isotropic mechanical reinforcement of polymeric composites. Recent works have reported the titanium oxide–reinforced PA12 composites with increased tensile strength, tensile modulus, and thermostability [25] and alumina-reinforced polystyrene composites that exhibited enhanced tensile and impact strength [26]. In addition to the mechanical reinforcement effect, the zinc oxide (ZnO) nanoparticles also exhibit multifunctionalities that find wide applications in photocatalysis, piezoelectric devices, gas sensors, and UV-protection [27–31]. ZnO-reinforced polymer composites also exhibit excellent biocompatibility and an antibacterial property [32]. However, research on metal oxide–based nanocomposite powders for the use in PBF techniques is relatively limited.

Herein, surface-modified ZnO nanorod–reinforced PA12 nanocomposite powders for MJF were developed. The synthesis and surface modification of ZnO nanorods were performed. The impacts of the nanofiller content on the crystallisation behaviour and the thermostability of the MJF-printed nanocomposites were systematically investigated. The filler distribution, mechanical properties, and facture mechanisms were analysed, with an emphasis on the uniform enhancements in the tensile and flexural properties of the MJF-printed ZnO-reinforced nanocomposites. This work integrates nanotechnology with the MJF technique to fabricate nanocomposites with uniformly enhanced mechanical performance through a facile and viable approach.

2. Materials and methods

2.1. Preparation of surface-modified ZnO nanorods

In this work, the ZnO nanorods were synthesized through a hydrothermal process and surface modified following the schematic shown in Figure 1a. Zinc nitrate hexahydrate ($Zn(NO_3)_2{\cdot}6H_2O$), sodium hydroxide (NaOH), and poly(diallyldimethylammonium chloride) (PDDA) were purchased from Sigma Aldrich. 27.84 g $Zn(NO_3)_2{\cdot}6H_2O$ and 23.04 g NaOH were mixed in 240 mL deionized water under magnetic stirring for 1 h. The synthesis maintained a hydrothermal temperature of 150 °C for 9 h in a Teflon-lined stainless-steel autoclave. Hereafter, the as-synthesised ZnO nanorods are referred to as ZnO for simplicity.

The ZnO were added to 0.2 mol/L PDDA solution, and the pH was adjusted to 12 with 2 mol/L NaOH solution. In an aqueous alkaline environment, ZnO tend to physically adsorb polar water molecules and form negatively charged zincate species through amphoteric reactions [33]. At pH 12, the $Zn(OH)^{3-}$ species predominates, which facilitates the bonding with PDDA. The white-coloured precipitates were collected, rinsed with distilled water, and dried. The surface-modified ZnO nanorods are hereafter referred to as SMZnO.

2.2. Composite powder preparation

The 3D Reusability PA12 powder developed by Hewlett-Packard (HP) Inc. was used as received. The PA12 molecular chains were end-capped, rendering them less prone to thermal aging. The melting temperature, particle size, bulk density, and cost of the powder feedstock are presented in Table S1 [34]. The mechanical mixing of (SM)ZnO with PA12 powder was conducted at filler loading fractions of 1, 3, and 5 wt% using a mechanical mixer (Inversina 2L, Bioengineering AG, Switzerland). The rotation speed was set at 60 rpm for a duration of 4 h. The mixed composite powders are referred to as *x* wt% (SM)ZnO/PA12, where *x* denotes the weight fraction of the ZnO nanorods.

2.3. MJF printing parameters

The MJF testbed developed by HP Inc. (USA) was employed to fabricate PA12 and (SM)ZnO/PA12 parts, where the printing parameters were tunable on demand. The components of the MJF testbed and the fusion process are illustrated in Figure 1b & c. The dog bone–shaped tensile bars and the flexural bars were positioned along (*Y* orientation) and perpendicular (*X* orientation) to the roller spreading direction for comparison of mechanical properties in different orientations. The heating system comprises of overhead IR lamps whose power can be adjusted on demand and preheat elements embedded in the print bed. After the print bed preheat temperature (160 °C) was reached, the print bed was lowered by one-layer

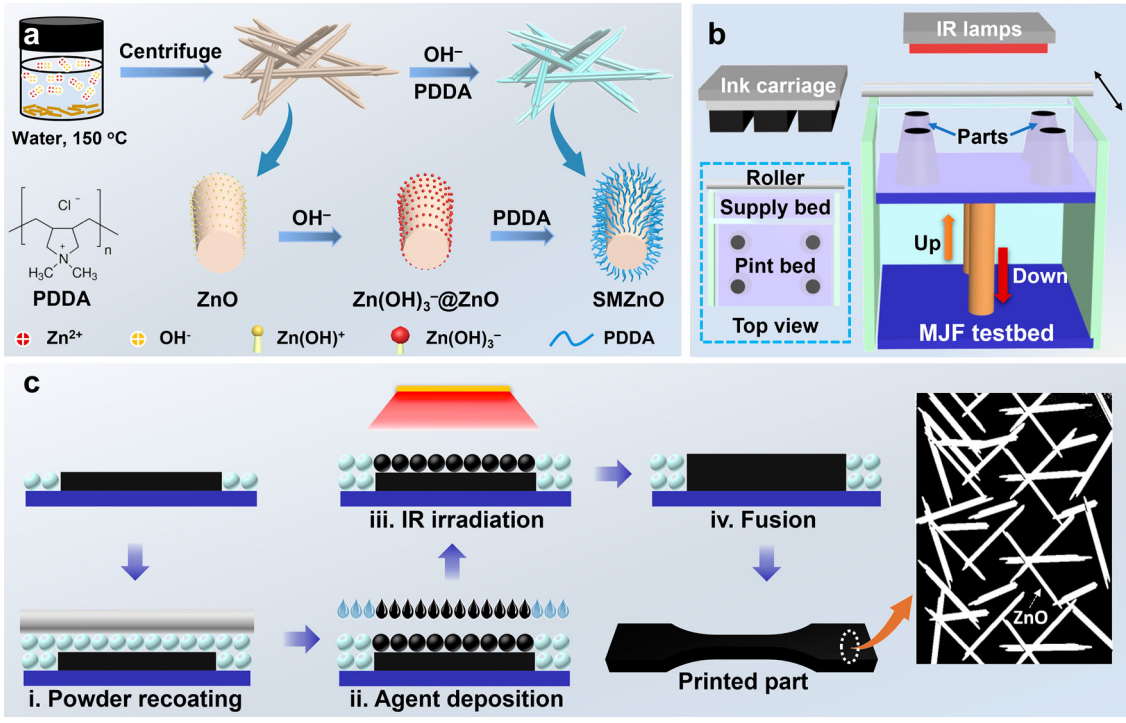

Figure 1. Synthesis of surface-modified ZnO nanorods and MJF printing of ZnO/PA12 nanocomposites. Schematics showing the (a) synthesis and surface modification of ZnO nanorods; (b) components of the MJF testbed; (c) MJF fusion process consisting of four steps: (i) powder recoating, (ii) agent deposition, (iii) IR irradiation, and (iv) fusion.

thickness, which was set at 80 µm in this study. A layer of powder was recoated onto the print bed by a counter-rotating roller at a rotational speed of 200 mm/s. The cartridge containing the inkjet system moved across the print bed at a speed of 16 inch/min, depositing the FA (developed by HP Inc. USA) within the designated regions. The heating lamps deliver thermal energy to the whole print bed while regions deposited with the FA absorbed the thermal energy, heated up to 210–220 °C, and caused powder in those regions to fuse. After finishing printing one layer, the print bed moved down by one layer thickness, and the supply bed moved up a distance corresponding to the supply ratio, which was set at 1.8 in this study. The process repeated until the complete specimen was printed. The printed parts were cooled under the ambient conditions and cleaned by bead blasting. The MJF-printed PA12 nanocomposites are named as (SM)ZnO-*x*/PA12, where *x* denotes the weight fraction of the ZnO nanorods.

2.4. Characterisations

The morphology of the ZnO and SMZnO nanorods was observed by a scanning electron microscope (SEM, JSM-5600 LV, JEOL, Japan), and the elemental composition was measured by energy dispersive X-ray spectroscopy (EDS). The dimension distributions of the nanorods were measured with the software ImageJ by randomly selecting 300 nanorods that were fully legible in the SEM images. The functional groups on the ZnO nanorods were characterised by Fourier transform infrared (FTIR) spectroscopy (IR Prestige 21, Shimadzu, Japan). The crystallinity of ZnO nanorods was examined by X-ray diffractometry (XRD, Shimadzu 6000, Japan). The powder flowability was assessed by measuring the dynamic avalanche angles using a powder analyser (Revolution Powder Analyser, Mercury Scientific Inc. Switzerland) at a drum rotation speed of 0.6 r/min.

The MJF-printed (SM)ZnO/PA12 nanocomposites were cryogenically fractured. The filler distribution in the polymer matrix was examined by SEM imaging and EDS mapping (SEM, JSM-5600 LV, JEOL, Japan). The dynamic thermogravimetric analysis (TGA) of the PA12 and (SM)ZnO/PA12 composite parts was performed using TGA-Q500 (TA instrument, New Castle, DE). Approximately 10 mg specimen was heated at a heating rate of 10 °C/min from 50 to 800 °C under N_2 and air environments, respectively. Differential scanning calorimetry (DSC) was performed using DSC-Q200 (TA Instrument, UK) at a N_2 flow rate of 40 mL/min. Approximately 10 mg of the MJF-printed specimens were enclosed in an aluminium pan and heated to 250 °C at

a heating rate of 10 °C/min. The specimen was subsequently cooled to 20 °C at a cooling rate of 10 °C/min and reheated to 250 °C at 10 °C/min. The cooling curves and the reheated enthalpies were used to calculate the crystallinity properties of the PA12 composites.

The mechanical properties of the composite parts were tested with a universal tester (AGX 10 kN, Shimadzu Corp., Japan). The tensile and flexural properties were measured in accordance with the ASTM D638 Type V standard and the ASTM C393 standard, respectively, at a test speed of 10 mm/min. In both measurements, four specimens were measured for each composition, and the average and variance values were calculated. The fractured surfaces of (SM)ZnO/PA12 parts were sputter coated with a thin layer of gold and observed using SEM.

3. Results and discussion

3.1. Properties of ZnO nanorods

The representative SEM images of ZnO and SMZnO nanorods are shown in Figures 2ai, bi, S1ai, & S1bi, with the insets showing the elemental composition characterised by EDS. Both specimens consisted of smooth, needle-like structures that possessed high aspect ratios and narrowed at the ends. Nanoparticles of other shapes were not observed in the SEM images, indicating synthesised nanorods with a well-controlled size and shape. In the EDS spectrum of SMZnO, an additional C peak and an O peak with higher intensity were observed at 0.26 and 0.53 eV, respectively, as compared to that of the ZnO specimen. This suggests the surface decoration of the organic PDDA onto the ZnO nanorods.

The length distribution of the as-synthesised and surface-modified ZnO nanorods are illustrated in Figure 2aii & bii. The as-synthesised ZnO nanorods are in needle-like shapes with smooth surfaces, with an average length of 7.16 µm and an average width of 620 nm (with an aspect ratio of about 11.55) (Figures 2aii & S1aii). The average length and width of the surface-modified ZnO nanorods exhibited a significant size reduction and are 2.16 µm and 340 nm (with an aspect ratio of about 6.35), respectively (Figures 2bii & S1bii). This reduction in dimensions could be owing to the aqueous alkaline environment, in which the ZnO nanorods dissolve slightly [33].

XRD analysis was conducted with a Cu k_α radiation source (λ = 1.5418 Å) to investigate the crystal structures of the as-synthesised and surface-modified ZnO nanorods. As shown in Figure 2c, both specimens contained diffraction peaks at 2θ values at 32.2°, 34.7°, 36.6°, 47.8°, 56.9°, and 63.2°, which were assigned to (100), (002), (101), (102), (110), and (103) crystal planes, respectively. The characteristic XRD diffraction peaks and relative intensities matched with literature values, indicating a hexagonal wurtzite phase structure with space group P63mc (JCPDS no. 36–1451) [28]. The intensity of the (101) plane was maximum among those of all

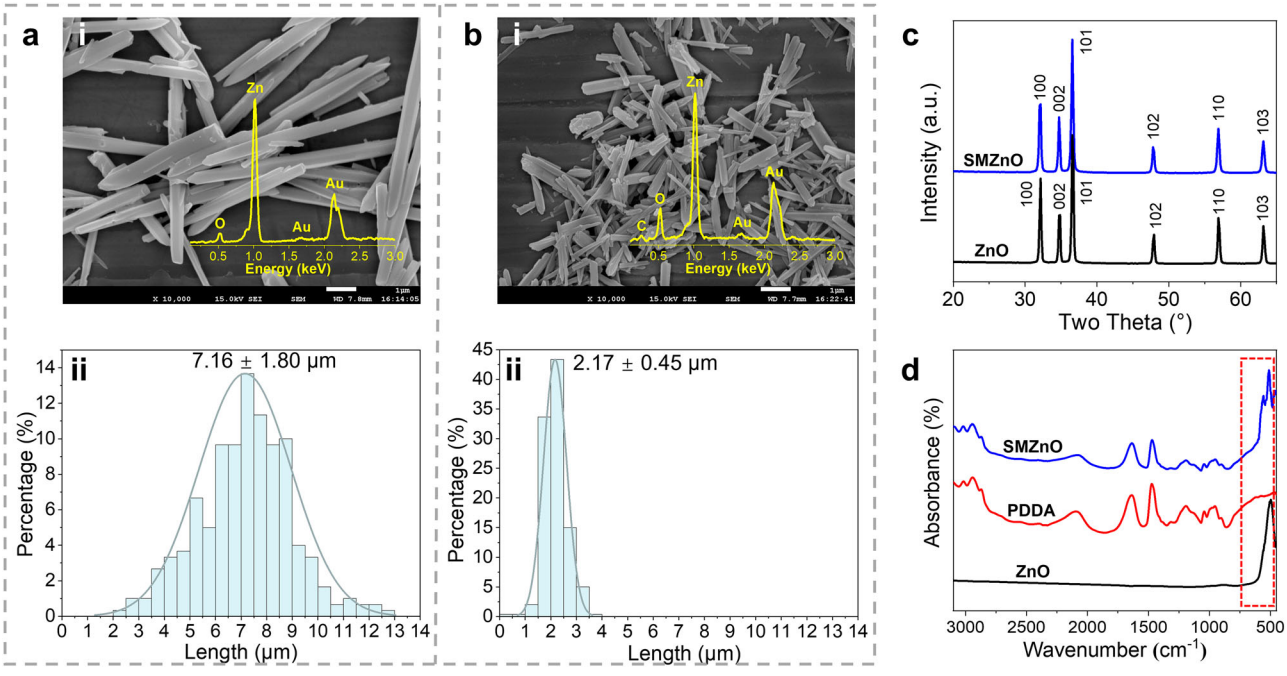

Figure 2. Characterisations of (SM)ZnO nanorods. (a) ZnO nanorods and (b) SMZnO nanorods: (ai, bi) SEM images with elemental composition and (aii, bii) nanorod length distribution; (c) XRD and (d) FTIR spectra of (SM)ZnO and PDDA.

diffraction peaks for both SMZnO and ZnO specimens, and its full width at half maximum (FWHM) was adopted to calculate the average crystallite size D, which was determined through the Scherrer's equation expressed as

$$D = \frac{0.89\ \lambda}{\beta \cos\theta}, \quad (1)$$

where λ is the X-ray wavelength, β is the FWHM, and θ is the Bragg diffraction angle (summarised in Table S2). The average crystallite sizes of ZnO and SMZnO were calculated to be 63 and 61 nm, respectively, indicating that the surface modification process had minimal effects on the crystallinity of ZnO [29,35].

The FTIR spectra of ZnO, PDDA, and SMZnO are shown in Figure 2d. The significant absorption peak at 497 cm^{-1} present in both ZnO and SMZnO spectra was assigned to the asymmetric Zn–O stretching vibration. Compared to the spectrum of ZnO, the SMZnO spectrum exhibited additional absorption bands at 2942 cm^{-1} (C–H), 1637 cm^{-1} (C=C), 1472 cm^{-1} (C–C), and 1193 cm^{-1} (C–N), which were the characteristics of PDDA [36,37], with the detailed peak attributions shown in Table S3. These values suggest the successful surface decoration of PDDA onto the ZnO nanorods.

3.2. Powder flowability

For the various PBF techniques, powder flowability is an essential attribute of the powder feedstock that affects the quality of the recoated layers, especially in composite powders with reinforcement fillers. Granulate specimens of good flowability are able to form dense, uniform recoated powder layers. Poor uniformity in the recoated powder layer leads to the formation of undesired defects or voids and thus the deterioration of the mechanical properties of the printed specimens [38]. The powder flowability of the (SM)ZnO/PA12 nanocomposite powders was characterised by measuring the dynamic avalanche angle, which is defined as the angle of the slope at which the powder specimen stabilises and comes to rest while the rotational drum is in motion. The schematic of the dynamic avalanche angle measurement is shown in Figure S2a. Small dynamic avalanche angles are indicative of powder materials with good flowability.

Both the ZnO/PA12 and SMZnO/PA12 nanocomposite powders exhibited low dynamic avalanche angles and satisfactory powder flowability. As shown in Figure 3, the ZnO/PA12 nanocomposite powders exhibited median avalanche angles of 51.97°, 55.13°, and 55.42°, respectively for 1, 3, and 5 wt% ZnO/PA12 powders, exhibiting slightly deteriorated powder flowability compared to that of the neat PA12 powder (46.18°, shown in Figure S2b). The SMZnO/PA12 nanocomposite powders exhibited lower median avalanche angles of 48.97°, 47.82°, and 50.76° for 1, 3, and 5 wt% SMZnO loading fractions, respectively, indicating improved powder flowability. It is worth noting that the dynamic avalanche angles of 1 and 3 wt% SMZnO/PA12 powders were comparable to that of the neat PA12 powder, indicating their exceptionally similar processing conditions. The improved powder flowability may be owing to the enhanced nanofiller–polymer compatibility as a result of the surface modification process. Nevertheless, all (SM)ZnO/PA12 nanocomposite powders exhibited median dynamic avalanche angles within the optimal processing range of 40°–60°, which has been empirically validated to ensure good printability for the polymer printing *via* MJF and other polymeric PBF processes [13,17,18,38].

3.3. ZnO nanorod distribution in the PA12 matrix

Polymer composites that contain large quantity of homogeneously distributed nanofillers often demonstrate superior mechanical properties [39]. Nanofillers, with large surface areas, create substantial filler–polymer interfaces, which aid the stress transfer during fracture and enhance the mechanical properties at low nanofiller loading fractions [23,26,31]. However, at high concentrations, the nanofillers tend to aggregate because of the high free surface energy, forming agglomerations within the polymer matrix and disrupting the matrix continuity [31,40].

Figures 4a–d and S3 show the SEM images of the cryogenically fractured morphology of (SM)ZnO/PA12 composites, with the insets showing the fractured morphology at a lower magnification. As the loading fraction of SMZnO increased from 1 to 5 wt%, the quantity of ZnO nanorods that were exposed by the fracture process increased, as illustrated by the rod-like structures highlighted by the yellow dotted circles. It is worth noting that no obvious nanofiller agglomeration was observed in the SMZnO/PA12 specimens up to a 3 wt% loading fraction, which was also confirmed by the corresponding EDS mapping (Figure S4). Owing to the small sizes of (SM)ZnO nanorods, they can be distributed in the voids between PA12 powder particles, which weakened or eliminated the shear-induced alignment of short fibres. The nanorods showed no preferential alignment in the polymer matrix, which complied with the simulated nanofiller distribution as shown in Figures S5 & S6.

However, the ZnO-5/PA12 composite part exhibited evident nanofiller agglomeration as illustrated by the

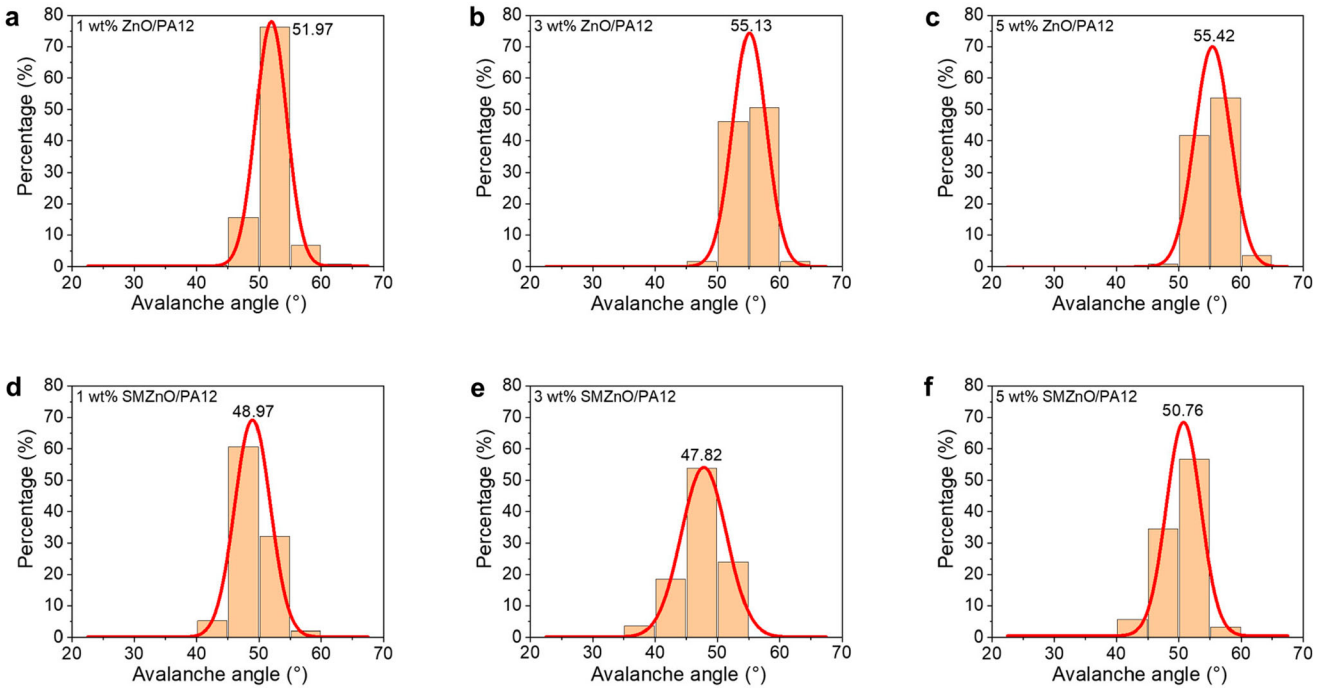

Figure 3. Dynamic avalanche angle measurement with Gaussian fit of composite PA12 powders loaded with (a) 1 wt%, (b) 3 wt%, (c) 5 wt% ZnO, (d) 1 wt%, (e) 3 wt%, and (f) 5 wt% SMZnO.

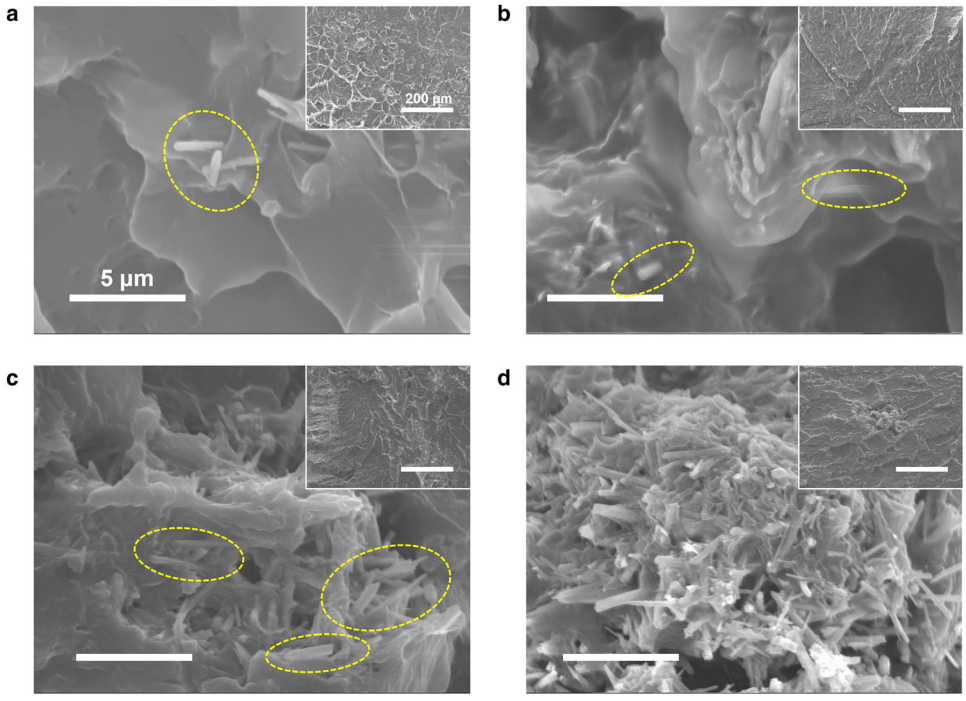

Figure 4. Nanofiller distribution in the PA12 matrix. SEM images of the cryogenically fractured surfaces of the ZnO/PA12 nanocomposite specimens with (a) 1 wt%, (b) 3 wt%, and (c) 5 wt% SMZnO and (d) 5 wt% ZnO.

cluster of nanorods shown in Figure 4d. Additionally, the EDS mapping images further revealed that the ZnO nanorods in the ZnO-5/PA12 composite part formed apparent clumps (Figure S5). The agglomeration of nanofillers disturbed the continuity of the polymer matrix and thus caused local stress concentrations at such sites. As the ability of the matrix to withstand loads deteriorated, the UTS reduced.

The enhanced homogeneity in the nanofiller dispersion was attributed to the surface modification process, where the aromatic ammonium groups on the PDDA molecules bonded with the $-NH_2$ groups on the PA12 polymer chains. The PDDA served to increase the distance between the quaternary ammonium bond on the ZnO nanorods, leading to a decrease in the binding surface activity and facilitating the nanofiller dispersion in the molten PA12 fusion pool during the MJF printing process [25,41].

3.4. Thermostability

The thermostability of the MJF-printed (SM)ZnO/PA12 composites was assessed by TGA performed under both the N_2 and air environments. The MJF-printed neat PA12 specimens exhibited good thermostability as evidenced by the high initial degradation temperature T_i, which is the temperature at 5% weight loss. The T_i value for neat PA12 was 391.85 °C in N_2 and 396.44 °C in air. The residue weight was 1.15%, indicating that the PA12 specimens underwent pyrolysis at high temperature [42]. The thermogravimetric results of the (SM)ZnO/PA12 composites are presented in Figure 5 and Table 1.

Under the N_2 atmosphere, the ZnO nanorods caused a consistent increase in T_i from 391.85 °C for the neat PA12 specimen to over 421 °C for all the PA12 nanocomposite specimens. A substantial increase was also observed in the half degradation temperature T_{half}, which is the temperature at 50% weight loss. The PA12 nanocomposites with the same filler loading fraction exhibited similar T_{half} values regardless the surface modification process. The elevated T_i and T_{half} values suggested the delayed thermal degradation and the enhanced thermostability of the ZnO/PA12 nanocomposites. The temperature at the maximum pyrolysis rate T_{max} is illustrated by the temperature corresponding to the peak of the derivative thermogravimetry (DTG) curve. As shown in Figure 5c, ZnO nanorods caused the increase in the T_{max} values, indicating the delay of the pyrolysis process. The residue weight of the PA12 composite specimens was 1.69% for the SMZnO-1/PA12 specimen and 5.09% for the SMZnO-5/PA12 specimen.

The oxidative degradation resistance of the PA12 composites was evaluated by TGA under the air atmosphere (Figure 5b & d). The parameters T_i, T_{half}, T_{max}, and residue weight followed a similar trend as those observed in the N_2 atmosphere. ZnO and SMZnO

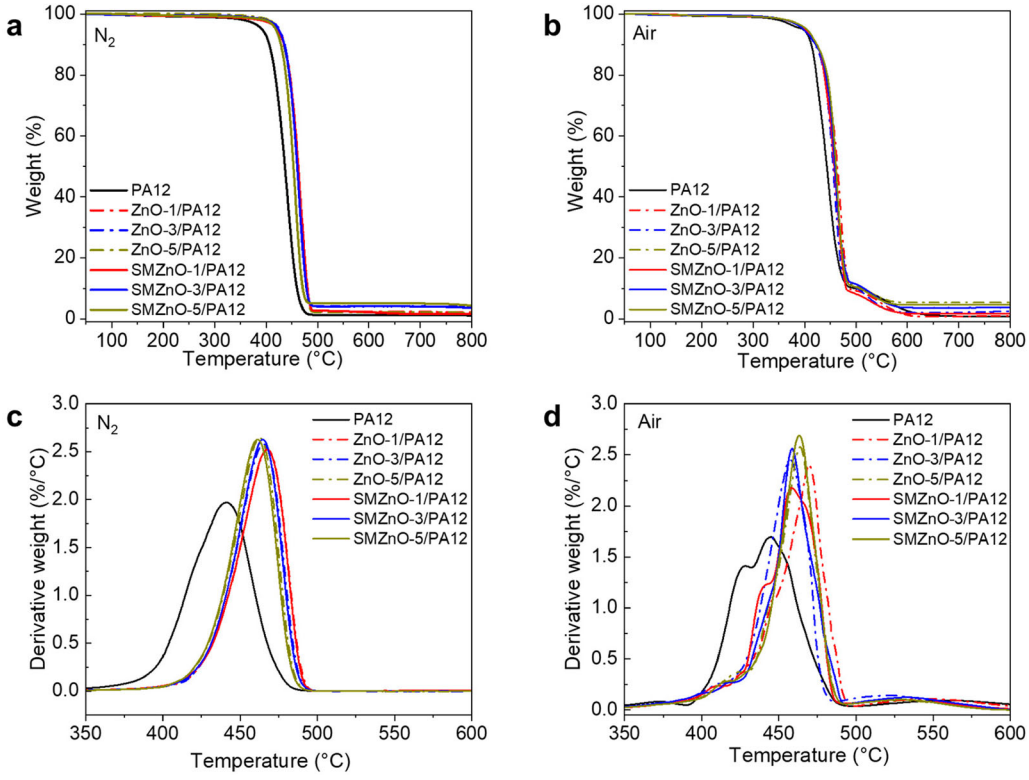

Figure 5. Thermostability results. TGA curves in (a) N_2 and (b) air and DTG curves in (c) N_2 and (d) air of (SM)ZnO/PA12 parts.

nanorods effectively delayed the pyrolysis process and increased the T_i, T_{half}, and T_{max} values. In summary, the (SM)ZnO nanorods enhanced both the thermostability and oxidative resistance of the PA12 composites.

3.5. Non-isothermal crystallisation behaviour

Crystallinity is an essential attribute of semicrystalline polymers as higher crystallinity is usually correlated to higher mechanical strength and thermostability. DSC analysis was employed to examine the heat flow profiles and study the effect of (SM)ZnO on the melting and crystallisation behaviour of the MJF-printed PA12 composites. The DSC curves, relative crystallinity plots, Avrami plots, and the crystallization rate analysis of (SM)ZnO/PA12 specimens are presented in Figures 6, S7 & Table 2.

Both the neat and (SM)ZnO-reinforced PA12 composites showed melting temperatures T_m at approximately 179°C with minimal deviations as shown by the prominent endothermic peaks in Figures 6a & S7a. The crystallisation temperature T_c of the (SM)ZnO/PA12 composites increased as the filler concentration increased, as evident in the shift of exothermic peaks in Figures 6b & S7b. The increased T_c values suggested a promoted recrystallisation process with the addition of nanofillers. The T_c values of the PA12 composites with the same filler loading fractions are comparable for PA12 composites regardless of the surface modification process, indicating that the surface modification of nanofillers had a negligible effect on the crystallisation behaviour of the PA12 matrix.

The melting enthalpy ΔH_m, which is computed by the integrated area of the heat absorption peaks, increased with the addition of ZnO and SMZnO fillers. The

Table 1. TGA and DTG results under N_2 and air flow conditions.

	T_i (°C)		T_{half} (°C)		T_{max} (°C)		Residue weight (%)	
Specimen	N_2	Air	N_2	Air	N_2	Air	N_2	Air
PA12	391.85	396.44	436.68	443.28	441.18	445.21	1.15	0.89
ZnO-1/PA12	424.26	382.46	462.80	464.01	467.64	470.06	2.13	1.05
ZnO-3/PA12	425.60	399.43	461.29	455.58	465.29	457.41	3.82	2.51
ZnO-5/PA12	423.68	403.79	459.18	461.10	462.86	463.66	4.19	5.42
SMZnO-1/PA12	421.54	401.33	462.51	457.86	467.50	458.17	1.69	1.72
SMZnO-3/PA12	424.20	397.55	460.89	459.06	464.72	458.59	3.64	3.70
SMZnO-5/PA12	423.19	403.93	458.35	461.27	456.74	463.19	5.09	4.66

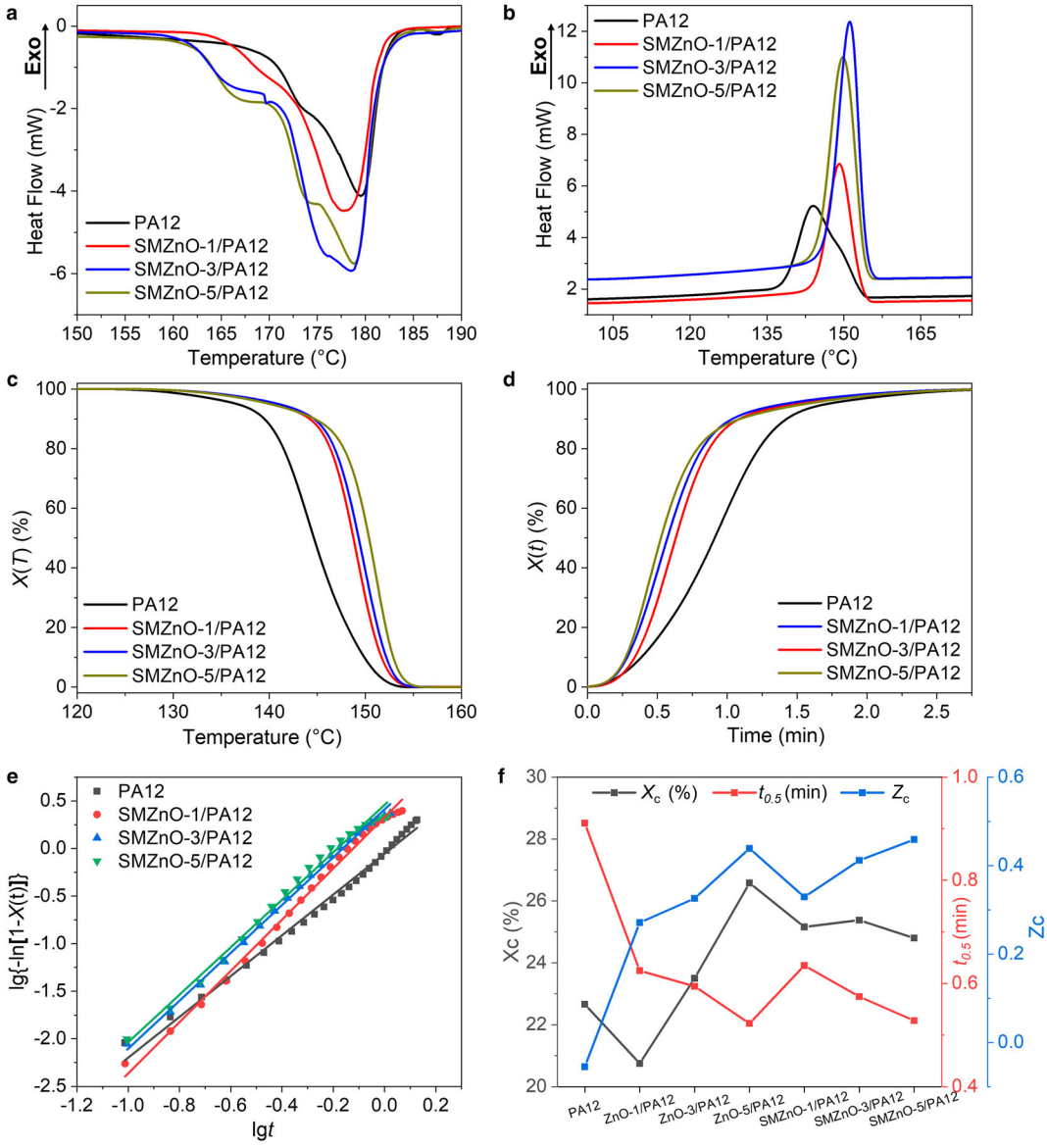

Figure 6. Non-isothermal crystallisation studies. DSC (a) melting and (b) cooling curves of SMZnO/PA12 composites; relative crystallinity plotted as a function of (c) temperature and (d) time; (e) Avrami plots and (f) X_c, $t_{0.5}$, and Z_c values of the SMZnO/PA12 composites.

degree of crystallinity X_c in relation with ΔH_m can be calculated by

$$X_c = \frac{\Delta H_m}{\Delta H_m^0 (1 - w)} \times 100\%, \quad (2)$$

Table 2. Non-isothermal crystallisation parameters of (SM)ZnO/PA12 composites measured by DSC.

Specimen	X_c (%)	T_m (°C)	T_c (°C)	$t_{0.5}$ (min)	Z_c
PA12	22.66	179.54	144.00	0.91	−0.05
ZnO-1/PA12	20.75	177.98	148.55	0.62	0.27
ZnO-3/PA12	23.50	178.14	150.01	0.59	0.33
ZnO-5/PA12	26.58	179.51	151.47	0.52	0.44
SMZnO-1/PA12	25.16	177.81	149.12	0.63	0.33
SMZnO-3/PA12	25.38	178.80	149.84	0.57	0.41
SMZnO-5/PA12	24.80	178.47	151.17	0.53	0.46

where ΔH_m^0 is the enthalpy of fully crystalline PA12 (209.3 J/g), and w is the fraction of nanorods in the composites. The (SM)ZnO/PA12 composites exhibited higher X_c than that of their neat PA12 counterparts owing to the addition of (SM)ZnO nanorods, which acted as heterogeneous nucleation sites and promoted the crystallisation of the semi-crystalline PA12 matrix [42]. The SMZnO/PA12 specimens exhibited higher X_c than that of those reinforced with untreated ZnO nanorods, probably owing to the improved dispersion of fillers in the PA12 fusion pool as a result of the surface modification [43].

The relative crystallinity of PA12 nanocomposites was plotted as a function of temperature T (Figure 6c) to evaluate the effect of SMZnO filler addition on the

crystallisation rate of the PA12 matrix. The $X(T) - T$ relation was expressed as the ratio of the area of the crystallisation peak integrated until the temperature T to the total integrated area (until $T = \infty$), given by

$$X(T) = \frac{\int_{T_0}^{T} (\mathrm{d}H_c/\mathrm{d}T)\mathrm{d}T}{\int_{T_0}^{T_\infty} (\mathrm{d}H_c/\mathrm{d}T)\mathrm{d}T}, \quad (3)$$

where H_c is the crystallization enthalpy. The crystallisation onset temperature $T_{c,onset}$ obtained from the $X(T)$ plot. The $T_{c,onset}$ values increased with the increasing SMZnO nanorod content, reaffirming the enhanced heterogeneous nucleation and crystallisation of the PA12 matrix.

Further manipulations were performed to match the Avrami equations. The crystallisation time t was calculated by

$$t = \frac{|T_{c,onset} - T(t)|}{\Phi}, \quad (4)$$

where $T(t)$ is the temperature at time t, and Φ is the cooling rate. Through this manipulation, the $X(T) - T$ graph was transformed into the $X(t) - t$ plot as shown in Figure 6d. The half crystallisation time $t_{0.5}$ (the time at which 50% crystallinity) was achieved and is presented in Figure 6f. It exhibited a similar trend to T_c, whereby the $t_{0.5}$ values decreased with an increasing filler concentration. This relation indicates that the higher the SMZnO filler concentration, the faster the crystallisation process.

The crystallisation kinetics are analysed by the modified Avrami equation

$$\lg\{-\ln[1 - X(t)]\} = n \lg t + \lg Z_t \quad (5)$$

and

$$\lg Z_c = \frac{\lg Z_t}{\Phi} \quad (6)$$

with the Avrami kinetic component n and the overall kinetic rate constant Z_c being the slope and the intercept, respectively. The Avrami plots of the SMZnO/PA12 and ZnO/PA12 composites are shown in Figures 6e & S7e. The Z_c values increased as the (SM)ZnO nanofiller content increased, indicating an accelerated crystallisation process which agrees with the $t_{0.5}$ analysis.

In summary, the (SM)ZnO fillers enhanced the crystallinity and crystallisation rates of the PA12 composites. A higher nanofiller loading was correlated to a higher degree of crystallinity and a faster crystallisation rate.

3.3. Mechanical performance

3.3.1. Tensile performance

The tensile properties of the MJF-printed (SM)ZnO/PA12 composites are illustrated in Figure 7 and listed in Table S4. Both the UTS and Young's modulus of the (SM)ZnO/PA12 composites exhibited apparent improvements with magnitudes comparable in both *X* and *Y* orientations. The SMZnO nanofiller exhibited more apparent mechanical enhancements than their unmodified counterparts.

As illustrated in Figure 7a–c, the UTS of the MJF-printed ZnO-reinforced PA12 composites exhibited an increasing trend up to a 3 wt% nanofiller loading fraction. Compared to the UTS of the neat PA12 specimen, that of the ZnO-3/PA12 nanocomposite increased from 48.51 to 58.23 MPa along the *X* orientation and from 49.62 to 59.62 MPa along the *Y* orientation. As the loading fraction of nanofillers increased, a large number of filler–matrix interfaces are formed, which led to mechanical strengthening of the PA12 composites [44,45]. Another factor contributing to the enhanced UTS at high nanofiller loading fractions is the high crystallinity revealed by the DSC analysis.

Nevertheless, a further increase in the unmodified ZnO loading fraction led to the deterioration of the UTS. The ZnO-5/PA12 specimen exhibited a slightly decreased UTS of 56.23 MPa along the *X* orientation and 57.92 MPa along the *Y* orientation. This decrease is owing to the inevitable nanofiller agglomeration, which disrupted the polymer matrix continuity and thus led to abrupt matrix failures at low elongation [23,31]. Moreover, the nanofiller agglomeration significantly reduced the formation of filler–matrix interfaces, thereby leading to less effective stress transfers and subsequentially impaired mechanical integrity.

The SMZnO nanorods demonstrated a significant enhancement in the tensile properties of the MJF-printed PA12 composites compared to that of ZnO/PA12. This enhancement can be primarily attributed to the improved interfacial adhesion between the filler and matrix materials. As shown in Figure 7, the UTS of SMZnO-3/PA12 (64.07 MPa) was 29.12% higher than that of the neat PA12 specimen oriented along the *Y* orientation, compared to a 20.15% increase by their untreated counterparts (59.62 MPa). Similarly, the UTS of SMZnO-3/PA12 and ZnO-3/PA12 in the *X* orientation were 62.02 and 58.23 MPa, respectively, which were 27.85% and 20.04% higher than that of the neat PA12 specimen. This increase can be attributed to the enhanced interfacial adhesion strength between the filler and the polymer matrix and the reduced filler agglomeration.

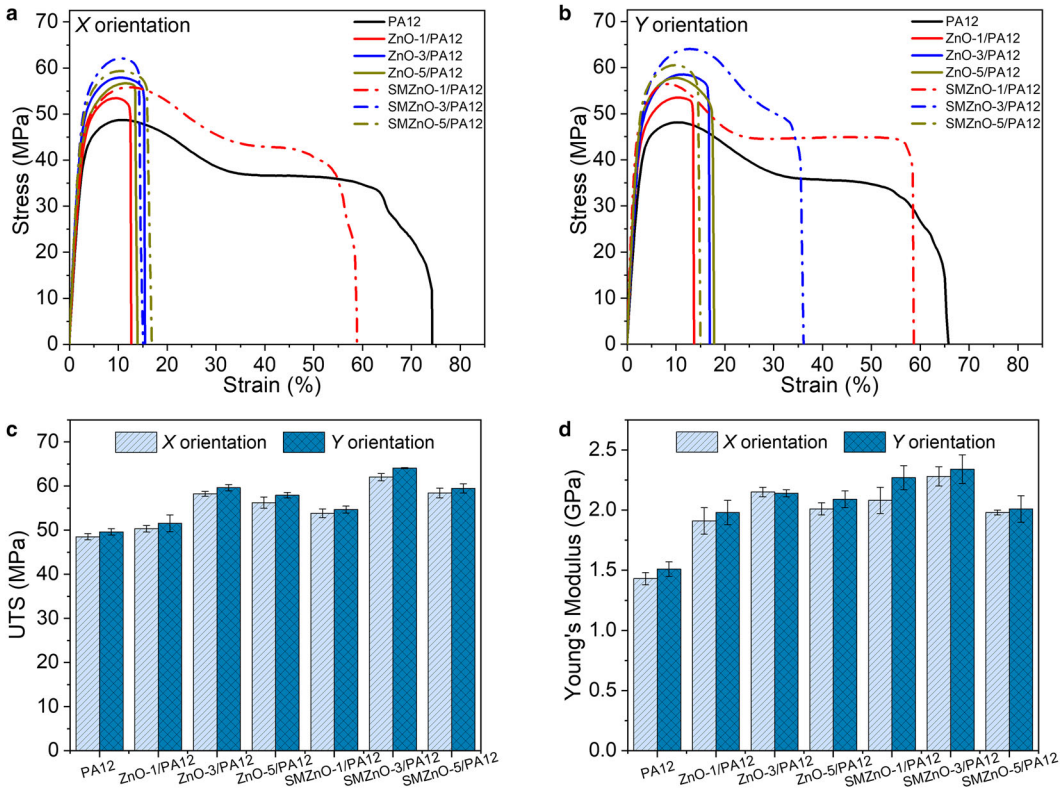

Figure 7. Tensile properties of (SM)ZnO/PA composites. Tensile stress–strain measured along the (a) *X* and (b) *Y* orientations; (c) UTS and (d) Young's modulus of the (SM)ZnO/PA12 composites.

The Young's modulus of the (SM)ZnO/PA12 composites exhibited a similar trend as the UTS, as illustrated in Figure 7d. The Young's modulus of both ZnO/PA12 and SMZnO/PA12 composites peaked at a 3 wt% nanofiller loading fraction, which were 2.27 and 2.34 GPa, respectively. The addition of 3 wt% SMZnO led to a 59.44% increase in the Young's modulus, compared to a 50.35% increase in that of the ZnO-3/PA12 specimen, both measured along the *X* orientation.

As the filler loading fraction increased, the fracture mechanism of the PA12 nanocomposites transited from linear elastic deformation to pseudo-plastic deformation before the tensile stress reached the UTS [25,41]. As shown in the SEM images (Figures 8a, b, S8a, & S8b), the tensile fractured surfaces of MJF-printed (SM)ZnO-1/PA12 specimens exhibited numerous fibrils, indicating a typical ductile fraction mechanism. This is supported by the plastic deformation portion in the tensile curves of PA12 and SMZnO-1/PA12 composites (Figures 7a & b). Whereas at higher filler loading fractions, the fractured surfaces were flat, indicating insignificant plastic deformation (Figures 8c–f & S8c–f). The premature failure of (SM)ZnO-5/PA12 specimens may be owing to the increased quantity of fillers which served as local stress concentration sites, which caused matrix cracking and eventually failure. The fractographs of PA12 nanocomposites in both the *X* and *Y* orientations exhibited similar patterns, indicating similar and uniform reinforcement effects in both the *X* and *Y* orientations.

3.3.2. Flexural performance

The flexural strength and modulus of the MJF-printed (SM)ZnO/PA12 nanocomposites were improved by the reinforcement of nanofillers, as shown in Figure 9 and Table S4. It is worth noting that the flexural properties exhibited comparable enhancements in both the *X* and *Y* orientations. For PA12 specimens reinforced with untreated ZnO nanorods, both the flexural strength and modulus increased up to 3 wt% filler loading fraction and deteriorated at 5 wt%. The maximum flexural strength was 75.74 and 79.48 MPa in the *X* and *Y* orientations, respectively, indicating 40.04% and 43.65% increases compared to those of the neat PA12 specimens. The optimal flexural modulus was 1.48 and 1.66 MPa the *X* and *Y* orientations, respectively, equivalent to 8.03% and 16.90% increases as compared to those of the neat PA12 specimens.

In the PA12 specimens reinforced with SMZnO, the flexural properties increased as the filler loading fraction increased up to 5 wt%, suggesting stronger filler–matrix interactions and better filler–matrix compatibility. In the

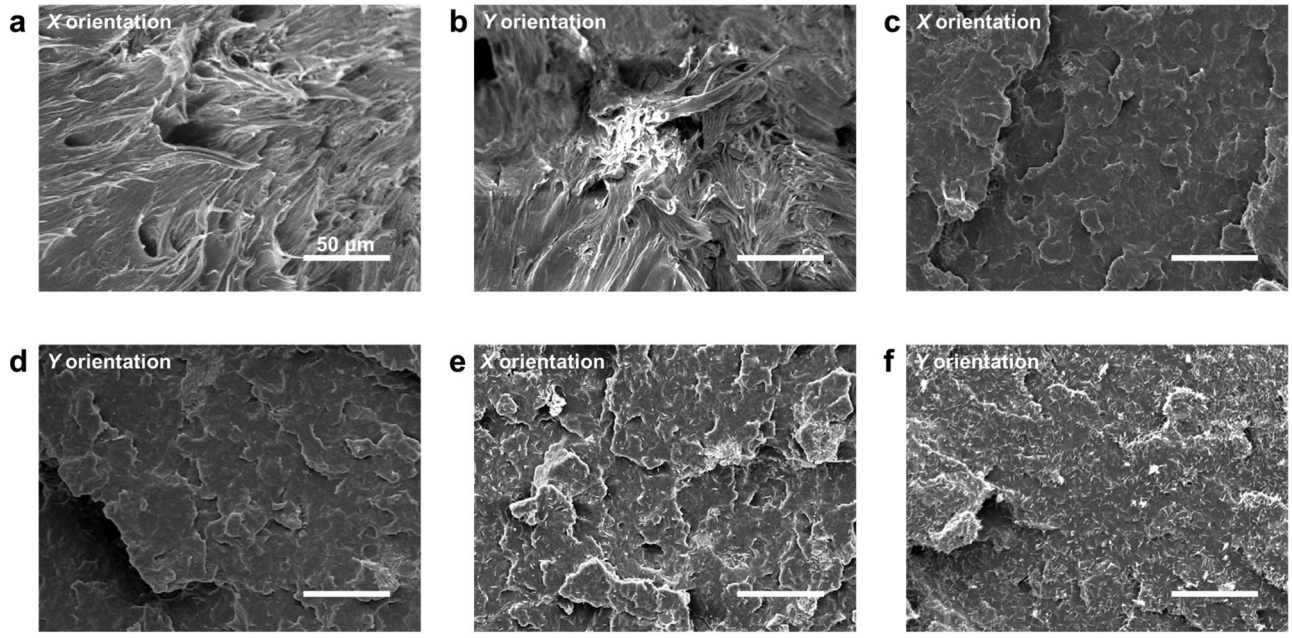

Figure 8. Fractured morphologies of SMZnO/PA12 specimens after tensile tests. SEM images of MJF-printed PA12 specimens with (a, b) 1 wt%, (c, d) 3 wt%, and (e, f) 5 wt% SMZnO in the (a, c, e) *X* and (b, d, f) *Y* orientations, respectively.

X orientation, the maximum flexural strength and modulus were 97.56 MPa and 1.91 GPa, respectively, equivalent to 42.65% and 34.51% increments, respectively (Figure 9a). The SMZnO-5/PA12 specimen exhibited the highest flexural strength and modulus, which were 92.68 MPa and 1.90 GPa, equivalent to

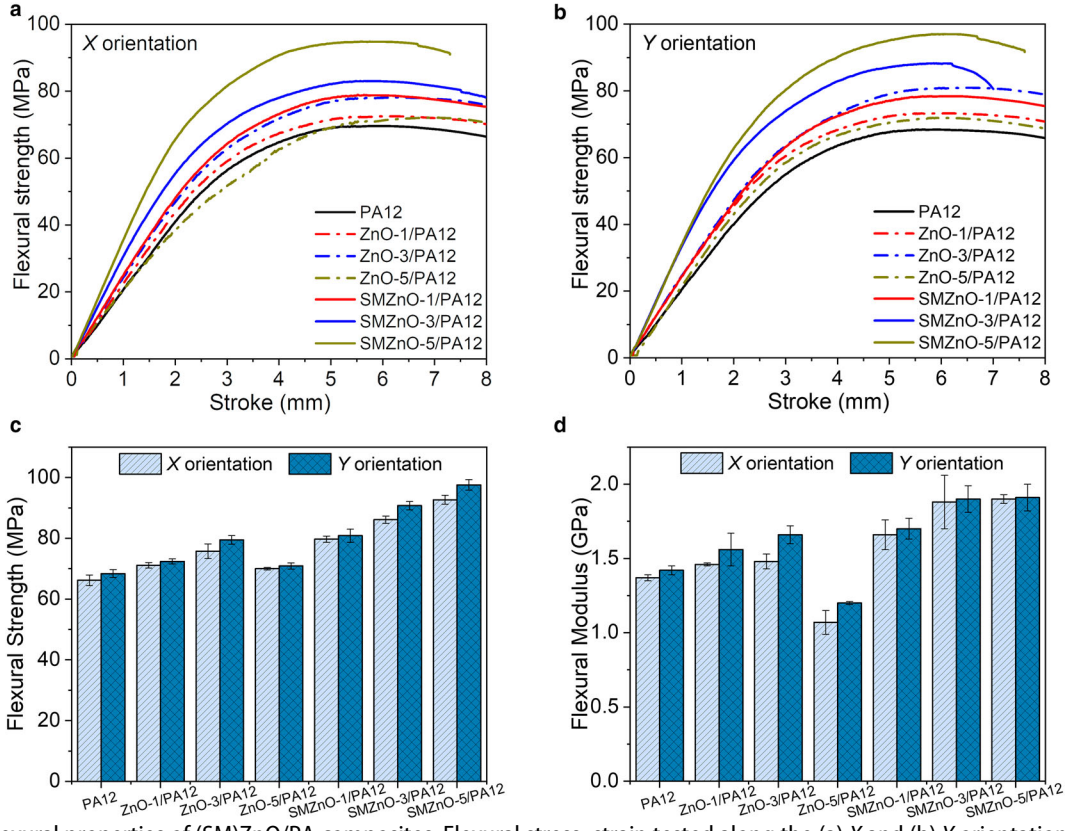

Figure 9. Flexural properties of (SM)ZnO/PA composites. Flexural stress–strain tested along the (a) *X* and (b) *Y* orientations; (c) flexural strength and (d) flexural modulus of the (SM)ZnO/PA12 composites.

Table 3. Tensile and flexural properties of MJF-printed PA12 composites reinforced with untreated and surface modified fillers.

	Filler	Filler content (wt %)	Surface modification		UTS (MPa)	Variation[a] (%)	Young's modulus (GPa)	Variation[a] (%)	Flexural strength (MPa)	Variation[a] (%)	Flexural modulus (GPa)	Variation[a] (%)	Ref
	N.A.	N.A.	N.A.	***X***	47.00	–	1.24	–	50.00	–	1.15	–	[46]
				Y	48.00	–	1.15	–	66.00	–	1.56	–	
Untreated	GB	40	N.A.	***X***	31.00	−34.04	2.20	76.97	50.00	0.00	1.80	56.72	[20]
				Y	31.00	−35.42	2.33	103.31	57.00	−13.64	2.30	46.52	
	GF	10	N.A.	***X***	42.20	2.43	1.13	−17.52	70.80	1.00	1.60	14.29	[14]
				Y	52.50	13.39	2.30	52.32	74.70	7.02	1.70	21.43	
	AF	6 (tensile) / 4 (flexural)	N.A.	***X***	45.29	−8.13	1.87	18.76	78.30	12.79	1.58	14.22	[18]
				Y	58.58	20.56	2.72	54.99	84.32	22.72	1.84	34.14	
	AF	12	N.A.	***X***	29.70	−35.64	1.49	−3.87	60.07	−4.42	1.47	6.52	[13]
				Y	60.61	27.44	4.71	178.70	88.45	36.67	2.34	82.81	
	PI fibre	8	N.A.	***X***	40.55	−13.74	1.25	−22.84	63.07	−0.32	1.22	−1.77	[19]
				Y	60.54	25.29	2.27	39.26	83.25	20.46	1.6	11.97	
Surface modified	GF	10	LDH [b]	***X***	47.80	16.02	2.51	83.21	86.4	23.25	1.8	28.57	[14]
				Y	63.70	37.58	3.55	135.10	98.7	41.4	2.3	64.29	
	GF	20	Silane coupling agent	***X***	48.24	−0.94	3.05	122.63	–	–	–	–	[16]
				Y	67.31	51.26	5.84	326.28	–	–	–	–	
	AF	6 (tensile) / 4 (flexural)	Fe_3O_4 [c]	***X***	52.99	7.48	2.20	39.42	82.96	19.50	1.73	24.77	[18]
				Y	65.70	35.21	3.24	84.44	90.24	31.33	2.15	56.53	
	AF	10	HBP [d]	***X***	40.74	−11.13	1.82	19.74	66.19	0.96	1.57	16.30	[17]
				Y	73.37	54.53	4.17	109.55	90.29	33.01	2.52	71.43	
	ZnO	3 (tensile) / 5 (flexural)	PDDA [e]	***X***	62.02	27.85	2.28	59.44	92.68	40.04	1.90	38.69	This work
				Y	64.07	29.12	2.34	54.97	97.56	42.65	1.91	34.51	

[a]Variation relative to those of the neat PA12 parts; [b] LDH: layered double hydroxides; [c] Fe_3O_4: iron oxide; [d] HBP: hyperbranched polyamide; [e] PDDA: poly(diallyl dimethylammonium chloride).

40.04% and 38.69% increments as compared to those of the neat PA12 specimens, respectively, along the *Y* orientation (Figure 9b).

3.3.3. Comparison of mechanical properties

To emphasize the benefits of the uniform mechanical enhancements caused by the incorporation of SMZnO, the tensile and flexural performances of previously reported MJF-printed PA12 composites are listed in Table 3.

The addition of large quantity (40 vol%) of spherical GBs to the PA12 powder caused compromised UTS and flexural strength, in both the *X* and *Y* orientations, while achieving enhanced tensile and flexural moduli. The short-shopped fibre–reinforced PA12 composites demonstrated notable mechanical anisotropy, characterised by the enhanced tensile and flexural properties along the *Y* orientation, albeit at the expense of sacrificed mechanical properties in the *X* orientation. In contrast, the SMZnO/PA12 nanocomposites reported in this work exhibited uniform improvements in the UTS, Young's modulus, flexural strength, and flexural modulus, along both the *X* and *Y* orientations, at a low filler loading fraction. It is worth noting that the flexural strength and modulus of SMZnO-5/PA12 nanocomposites outperformed most of the currently reported MJF-printed PA12 composites.

4. Conclusions

This work presents a facile bottom-up approach to fabricate ZnO nanorod–reinforced PA12 nanocomposites *via* the MJF technique for uniformly enhanced mechanical properties at a low nanofiller loading fraction. A surface modification method was developed to further reduce nanofiller agglomeration and improve the interfacial adhesion between the nanofiller and the PA12 matrix, thereby achieving the desired mechanical enhancements. The (SM)ZnO/PA12 composites exhibited effectively enhanced thermostability and higher crystallisation compared to those of the neat PA12 specimen. The UTS and Young's modulus of SMZnO-3/PA12 composite reached 62.02 MPa and 2.28 GPa in the *X* orientation, and 64.07 MPa and 2.34 GPa in the *Y* orientation. The flexural strength and modulus for SMZnO-5/PA12 were 92.68 MPa and 1.90 GPa in the *X* orientation, and 97.56 MPa and 1.91 GPa in the in the *Y* orientation. The MJF-printed SMZnO/PA12 nanocomposites exhibited uniform mechanical enhancements, rendering them suitable for applications that require structural complexity and cost effectiveness. The surface modification approach and nanotechnology can be potentially extended to other PBF techniques or processing techniques involving powder feedstocks for the fabrication of polymer composites with uniform mechanical enhancements.

Acknowledgements

This work was supported by the RIE2020 Industry Alignment Fund – Industry Collaboration Projects (IAF-ICP) Funding Initiative, Singapore and the cash and in-kind contributions from the industry partner, HP Inc.

Disclosure statement

No potential conflict of interest was reported by the author(s).

Funding

This work was supported by Industry Alignment Fund-Industry Collaboration Projects Grant: [Grant Number I1801E0028].

ORCID

Ran An http://orcid.org/0000-0001-8398-4700
Yanbei Hou http://orcid.org/0000-0002-6146-5122
Kun Zhou http://orcid.org/0000-0001-7660-2911

References

[1] Tan LJ, Zhu W, Zhou K. Recent progress on polymer materials for additive manufacturing. Adv Funct Mater. 2020;30(43):2003062.
[2] Liu Y, Sing SL. A review of advances in additive manufacturing and the integration of high-performance polymers, alloys, and their composites. Mater Sci Addit Manuf. 2023;2(3):1587.
[3] Tischer F, Cholewa S, Düsenberg B, et al. Polyamide 11 nanocomposite feedstocks for powder bed fusion via liquid-liquid phase separation and crystallization. Powder Technol. 2023;424:118563. doi:10.1016/j.powtec.2023.118563
[4] Chen P, Li Z, Liu S, et al. Preparation of polyamide 6 and its titanium dioxide photocatalytic composite powders for laser powder bed fusion. Mater Sci Addit Manuf. 2022;1. doi:10.18063/msam.v1i3.14
[5] Jansson A, Pejryd L. Characterisation of carbon fibre-reinforced polyamide manufactured by selective laser sintering. Addit Manuf. 2016;9:7–13. doi:10.1016/j.addma.2015.12.003
[6] Jing W, Hui C, Qiong W, et al. Surface modification of carbon fibers and the selective laser sintering of modified carbon fiber/nylon 12 composite powder. Mater Des. 2017;116:253–260. doi:10.1016/j.matdes.2016.12.037
[7] Morales-Planas S, Minguella-Canela J, Lluma-Fuentes J, et al. Multi Jet Fusion PA12 manufacturing parameters for watertightness, strength and tolerances. Materials (Basel). 2018;11(8):1472.
[8] Rosso S, Meneghello R, Biasetto L, et al. In-depth comparison of polyamide 12 parts manufactured by Multi Jet Fusion and Selective Laser Sintering. Addit Manuf. 2020;36:101713. doi:10.1016/j.addma.2020.101713

[9] Salmoria GV, Paggi RA, Lago A, et al. Microstructural and mechanical characterization of PA12/MWCNTs nanocomposite manufactured by selective laser sintering. Polym Test. 2011;30(6):611–615. doi:10.1016/j.polymertesting.2011.04.007
[10] Liao G, Li Z, Cheng Y, et al. Properties of oriented carbon fiber/polyamide 12 composite parts fabricated by fused deposition modeling. Mater Des. 2018;139:283–292. doi:10.1016/j.matdes.2017.11.027
[11] Heiderscheit T, Shen N, Wang Q, et al. Keyhole cutting of carbon fiber reinforced polymer using a long-duration nanosecond pulse laser. Opt Lasers Eng. 2019;120:101–109. doi:10.1016/j.optlaseng.2019.03.009
[12] Hupfeld T, Laumer T, Stichel T, et al. A new approach to coat PA12 powders with laser-generated nanoparticles for selective laser sintering. Procedia CIRP. 2018;74:244–248. doi:10.1016/j.procir.2018.08.103
[13] Chen J, Tan P, Liu X, et al. High-strength light-weight aramid fibre/polyamide 12 composites printed by Multi Jet Fusion. Virtual Phys Prototyp. 2022;17(2):295–307. doi:10.1080/17452759.2022.2036931
[14] Hou Y, Gao M, An R, et al. Surface modification of oriented glass fibers for improving the mechanical properties and flame retardancy of polyamide 12 composites printed by powder bed fusion. Addit Manuf. 2023;62(10):103195.
[15] Liu X, Tey WS, Choo JYC, et al. Enhancing the mechanical strength of Multi Jet Fusion–printed polyamide 12 and its glass fiber-reinforced composite via high-temperature annealing. Addit Manuf. 2021;46:102205.
[16] Liu X, Tey WS, Tan P, et al. Effect of the fibre length on the mechanical anisotropy of glass fibre–reinforced polymer composites printed by Multi Jet Fusion. Virtual Phys Prototyp. 2022;17(3):734–748. doi:10.1080/17452759.2022.2059638
[17] Chen J, Zhao L, Zhou K. Improvement in the mechanical performance of Multi Jet Fusion–printed aramid fiber/polyamide 12 composites by fiber surface modification. Addit Manuf. 2022;51:102205.
[18] Hou Y, Gao M, Chen J, et al. Preparation of iron oxide–coated aramid fibres for improving the mechanical performance and flame retardancy of Multi Jet Fusion–printed polyamide 12 composites. Virtual Phys Prototyp. 2023;18(1):e2171892.
[19] Chen M, Hou Y, An R, et al. Investigation of the mechanical properties of polyimide fiber/polyamide 12 composites printed by Multi Jet Fusion. Virtual Phys Prototyp. 2023;18(1):e2246032.
[20] Connor HJ O', Dowling DP. Comparison between the properties of polyamide 12 and glass bead filled polyamide 12 using the Multi Jet Fusion printing process. Addit Manuf. 2020;31:100961.
[21] El-Aty A A, Xu Y, Guo X, et al. Strengthening mechanisms, deformation behavior, and anisotropic mechanical properties of Al-Li alloys: a review. J Adv Res. 2018;10:49–67. doi:10.1016/j.jare.2017.12.004
[22] Yang Y, Song X, Li X, et al. Recent progress in biomimetic additive manufacturing technology: from materials to functional structures. Adv Mater. 2018;30(36):1706539. doi:10.1002/adma.201706539
[23] Rong MZ, Zhang MQ, Ruan WH. Surface modification of nanoscale fillers for improving properties of polymer nanocomposites: a review. Mater Sci Technol. 2006;22(7):787–796. doi:10.1179/174328406X101247
[24] Chen J, Zhu Y, Ni Q, et al. Surface modification and characterization of aramid fibers with hybrid coating. Appl Surf Sci. 2014;321:103–108. doi:10.1016/j.apsusc.2014.09.196
[25] Afshari M, Bakhshi S, Samadi M, et al. Optimizing the mechanical properties of TiO2/PA12 nano-composites fabricated by SLS 3D printing. Polym Eng Sci. 2023;63(1);267.
[26] Zheng H, Zhang J, Lu S, et al. Effect of core–shell composite particles on the sintering behavior and properties of nano-Al2O3/polystyrene composite prepared by SLS. Mater Lett. 2006;60:1219–1223. doi:10.1016/j.matlet.2005.11.003
[27] Aspoukeh PK, Barzinjy AA, Hamad SM. Synthesis, properties and uses of ZnO nanorods: a mini review. Int Nano Lett. 2022;12(2):153–168. doi:10.1007/s40089-021-00349-7
[28] Gupta J, Barick KC, Bahadur D. Defect mediated photocatalytic activity in shape-controlled ZnO nanostructures. J Alloys Compd. 2011;509(23):6725–6730. doi:10.1016/j.jallcom.2011.03.157
[29] Hong R, Pan T, Qian J, et al. Synthesis and surface modification of ZnO nanoparticles. Chem Eng J. 2006;119(2-3):71–81. doi:10.1016/j.cej.2006.03.003
[30] Ischenko V, Polarz S, Grote D, et al. Zinc oxide nanoparticles with defects. Adv Funct Mater. 2005;15(12):1945–1954. doi:10.1002/adfm.200500087
[31] Shiv JK, Kumar K, Jayapalan S. Recent advances in polymer using metal oxides nanocomposite and its hybrid fillers for tribological application. Adv Mater Process Technol. 2023: 1–12. doi:10.1080/2374068X.2023.2171673
[32] Li S-C, Li Y-N. Mechanical and antibacterial properties of modified nano-ZnO/high-density polyethylene composite films with a low doped content of nano-ZnO. J Appl Polym Sci. 2010;116(5):2965–2969. doi:10.1002/app.31802
[33] Degen A, Kosec M. Effect of pH and impurities on the surface charge of zinc oxide in aqueous solution. J Eur Ceram Soc. 2000;20(6):667–673. doi:10.1016/S0955-2219(99)00203-4
[34] Company HD. HP 3D high reusability PA12; 2019.
[35] Kumar SS, Venkateswarlu P, Rao VR, et al. Synthesis, characterization and optical properties of zinc oxide nanoparticles. Int Nano Lett. 2013;3(1):30. doi:10.1186/2228-5326-3-30
[36] Lam E, Hrapovic S, Majid E, et al. Catalysis using gold nanoparticles decorated on nanocrystalline cellulose. Nanoscale. 2012;4(3):997–1002. doi:10.1039/c2nr11558a
[37] Liu K, Zhang J, Yang G, et al. Direct electrochemistry and electrocatalysis of hemoglobin based on poly(diallyldimethylammonium chloride) functionalized graphene sheets/room temperature ionic liquid composite film. Electrochem Commun. 2010;12(3):402–405. doi:10.1016/j.elecom.2010.01.004
[38] Ziegelmeier S, Christou P, Wöllecke F, et al. An experimental study into the effects of bulk and flow behaviour of laser sintering polymer powders on resulting part properties. J Mater Process Technol. 2015;215:239–250. doi:10.1016/j.jmatprotec.2014.07.029

[39] Wu H, Fahy WP, Kim S, et al. Recent developments in polymers/polymer nanocomposites for additive manufacturing. Prog Mater Sci. 2020;111:100638.
[40] Yuan S, Shen F, Chua CK, et al. Polymeric composites for powder-based additive manufacturing: materials and applications. Prog Polym Sci. 2019;91:141–168. doi:10.1016/j.progpolymsci.2018.11.001
[41] Petousis M, Vidakis N, Mountakis N, et al. Three-Dimensional printed polyamide 12 (PA12) and polylactic acid (PLA) alumina (Al(2)O(3)) nanocomposites with significantly enhanced tensile, flexural, and impact properties. Nanomaterials (Basel). 2022;12(23):4292.
[42] Teo HWB, Chen K, Tran VT, et al. Non-isothermal crystallization behaviour of polyamide 12 analogous to multi-jet fusion additive manufacturing process. Polymer. 2021;235:124256.
[43] Lv W, Liu C, Ma Y, et al. Multi-hydrogen bond assisted SERS detection of adenine based on multifunctional graphene oxide/poly (diallyldimethyl ammonium chloride)/Ag nanocomposites. Talanta. 2019;204:372–378. doi:10.1016/j.talanta.2019.06.012
[44] Opelt CV, Becker D, Lepienski CM, et al. Reinforcement and toughening mechanisms in polymer nanocomposites – Carbon nanotubes and aluminum oxide. Composites, Part B. 2015;75:119–126. doi:10.1016/j.compositesb.2015.01.019
[45] Ajayan PM, Schadler LS, Braun PV. *Nanocomposite science and technology*. John Wiley & Sons; 2006.
[46] O'Connor HJ, Dickson AN, Dowling DP. Evaluation of the mechanical performance of polymer parts fabricated using a production scale Multi Jet Fusion printing process. Addit Manuf. 2018;22:381–387. doi:10.1016/j.addma.2018.05.035